Unravelling lithium distribution in carbon fibre electrodes for structural batteries with atom probe tomography

(article starts on next page)

Unravelling lithium distribution in carbon fibre electrodes for structural batteries with atom probe tomography

M. Johansen [a,**], M.P. Singh [b], J. Xu [a], L.E. Asp [a], B. Gault [b,c], F. Liu [a,*]
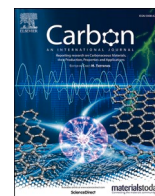
[a] *Department of Industrial and Materials Science, Chalmers University of Technology, 412 96, Gothenburg, Sweden*
[b] *Max-Planck-Institut für Eisenforschung GmbH, 40237 Düsseldorf, Germany*
[c] *Department of Materials, Imperial College London, London, SW7 2BP, UK*

ARTICLE INFO

ABSTRACT

Carbon fibres in structural batteries are multifunctional by acting both as structural reinforcement and as lithium (Li)-ion battery electrode. The relationship between the microstructure and mechanical capabilities of carbon fibres are well established, but much remains unexplored regarding their electrochemical properties. Specifically needed is a nanoscale understanding of how Li atoms distribute and interact in the carbon fibres. Atom probe tomography (APT) is uniquely positioned to provide subnanometre resolution in three dimensions. However, it has previously been hampered by undesirable Li migration during analysis. Here, we show that APT is successfully used to analyse electrochemically cycled polyacrylonitrile-based carbon fibres, through electrostatic shielding by means of conductive coating. We measure ~1.5 at% Li in the carbon fibres after full delithiation, and thus identify trapped Li to constitute a substantial part of the initial capacity fade. After lithiation, Li accounts for ~9 at% and according to frequency distribution analysis tend to agglomerate on the atomic scale. With nearest neighbour analysis, Li agglomeration is shown independent of heteroatom dopants such as nitrogen. Thus, the agglomeration is more likely induced by differing accessibility for Li in the crystalline and amorphous domains in the carbon fibre. The method used in this study can inform APT experiments on other type of Li-containing carbon electrodes. The findings of the study can be used to guide design of novel carbon fibres for structural batteries with enhanced electrochemical properties.

1. Introduction

Extending the range of electric transport demands energy storage systems to become lighter without compromising performance and durability. Structural batteries propose a solution based on multifunctionality by incorporating the energy storage function of lithium (Li)-ion batteries into carbon fibre reinforced composites and effectively reducing the required mass of the system [1–8]. In a conventional Li-ion battery, graphite is used as negative electrode material due to its low cost and ability to reversibly host Li ions. However, in a structural battery, carbon fibres act as negative electrode, while simultaneously performing the traditional role of carrying mechanical load. Therefore, carbon fibres that previously only have been developed to serve a structural purpose are now required to also perform electrochemically. The advancement of this new breed of multifunctional carbon fibres calls for a deeper understanding of their interplay with Li.

The electrochemical performance of carbon fibres has been extensively studied and proved promising with columbic efficiency of 99.9 % and specific capacities up to 350 mAh/g, which is close to the theoretical capacity of graphite at 372 mAh/g [9–12]. Carbon fibres have heterogenous microstructure of amorphous domains interspersed with crystalline phases of nanometre-sized crystallites of turbostratically stacked graphene layers [13,14]. Li can insert into either domain. It has been shown that compared with high modulus carbon fibres, the smaller crystallites in intermediate modulus carbon fibres are beneficial for enhanced electrochemical capacity [15]. Electrochemically cycled carbon fibres have been investigated with Raman spectroscopy [15], X-ray diffraction (XRD), nuclear magnetic resonance (NMR) [16], and Auger electron spectroscopy (AES) [17]. Among these, AES has the highest spatial resolution, in the nanometre range in the depth and lateral direction [18], and was successfully used to map Li distribution across a single fibre's full diameter (~5 μm). For slow lithiation the Li

---

* Corresponding author.
** Corresponding author.
    E-mail addresses: marcus.johansen@chalmers.se (M. Johansen), fang.liu@chalmers.se (F. Liu).

distribution was proved to be rather uniform on the microscale. For slow delithiation, the amount of present Li fell below the detection limit of AES.

Still, it is unknown how Li atoms are distributed in the nano-sized crystallites and amorphous domains in carbon fibres, and whether that distribution differs between states of full lithiation and full delithiation. Furthermore, the presence of N heteroatoms in intermediate modulus carbon fibres has been shown with hard X-ray photoelectron spectroscopy to be related to enhanced electrochemical performance [19]. However, the exact mechanism remains unknown – whether this effect originates from that Li coordinate more easily near N heteroatoms or N heteroatoms induce advantageous defects into the carbonaceous microstructure [20–28].

Capturing the nanoscale distribution of Li atoms requires high spatial resolution, which can be offered by electron energy loss spectroscopy (EELS) coupled to transmission electron microscopy (TEM) [29,30]. However, the electron beam can induce damages that affect distribution of light elements and more importantly EELS compresses three-dimensional information into two dimensions. Atom probe tomography (APT), on the other hand, has the capability to map individual atoms in three dimensions [31]. During APT analysis, a needle shaped specimen (tip radius ~50 nm) is deconstructed atom-by-atom through field evaporation induced by an electric field coupled with thermal activation by laser pulsing, where the atoms are ionised and emitted as positive ions. Based on the ion's time-of-flight and hit position at the detector, it is assigned a mass-to-charge ratio and a three-dimensional coordinate. From this information an atomic reconstruction of the specimen is generated and becomes possible to analyse with an array of digital tools. Previously, we revealed the microstructure of uncycled carbon fibres using APT [19,32]. Nevertheless, APT of materials containing Li is inherently challenging, as the electric field can drive Li migration [33–36]. Shielding the specimen with a thin layer of conductive metallic coating has been proposed and shown to prevent Li migration induced by electrostatic field penetration [35,37–39].

Here, we use APT to investigate the Li distribution in lithiated/delithiated polyacrylonitrile (PAN)-based T800 carbon fibres. We analyse specimens with and without shielding provided by an in-situ deposited metallic Cr coating. From APT analyses, we deduce that a significant part of the initial capacity fade comes from Li trapping in the carbon fibres. With frequency distribution analysis, we determine that the distribution of trapped Li in delithiated carbon fibres is uniform, whereas in lithiated fibres Li agglomerate. With nearest neighbour analysis, we show that the Li distribution is independent of the proximity to N heteroatoms, and instead related to the crystalline and amorphous domains. The insights brought forward by this study deepen the understanding of the interaction between Li and multifunctional carbon fibres and aid the development of tailored carbon fibres for structural batteries.

2. Material and method

PAN-based carbon fibre tows of type T800SC-12 k-50C with a linear weight of 0.52 g/m were supplied by Oxeon AB as unidirectional ultra-thin tapes. The tows were adhered to copper current collectors with conductive silver glue and stacked with 260 μm thick Whatman GF/A separator, and lithium metal. The material was soaked in electrolyte of 1.0 M LiPF$_6$, ethylene carbonate (EC), and diethyl carbonate (DEC) (EC: DEC 1:1 wt/wt, LP40 Sigma Aldrich) and encapsulated by pouch cell bags from Skultuna Flexible AB, Sweden. Cells were assembled in a dry argon atmosphere in a glovebox (<1 ppm H$_2$O, <1 ppm O$_2$). A Neware CT-4008-5V10mA-164 battery cycler was used to charge/discharge the cells for five cycles to either 0 % or 100 % state of charge. The potential window was 1.5 V–0.01 V versus Li/Li$^+$ and the current corresponded to 0.1C relative a theoretic graphite capacity of 372 mAh/g.

Four atom probe tomography (APT) instruments were used: LEAP 3000X HR and CAMECA LEAP 6000 XR at Chalmers University of Technology in Gothenburg, Sweden, and CAMECA LEAP 5000 XR and CAMECA LEAP 5000 XS at the Max-Planck-Institut für Eisenforschung GmbH in Düsseldorf, Germany. The LEAP 3000X HR was used for investigation of uncycled and lithiated carbon fibres, 6000 XR for uncycled carbon fibres, and 5000 XR and XS for both lithiated and delithiated carbon fibres.

At Chalmers University of Technology, the fibres were briefly exposed to ambient air during transport to a FEI Versa 3D dual-beam focused ion beam/scanning electron microscope (FIB/SEM) for APT specimen preparation [19,32], and then again briefly exposed to ambient air during transport to the atom probe instruments. For 3000X HR, data was acquired for lithiated carbon fibres at a base temperature of 100 K, a laser pulse energy of 1 nJ (wavelength λ = 532 nm), and a detection rate of 2 ions per 1000 pulses. Out of ten tips, only one yielded useful data before fracture. For 6000 XR, data was acquired for uncycled fibres at a base temperature of 100 K, a laser pulse energy of 150 pJ (λ = 258 nm), and a detection rate of 2 ions per 1000 pulses. Out of five tips, three yielded useful data before fracture.

At the Max-Planck-Institut für Eisenforschung, the fibres were either transported through ambient air or via an ultra-high vacuum transfer suitcase Ferrovac VSN-40. A Thermo-Fisher Helios5CX dual-beam FIB/SEM was used for specimen preparation [19,32]. The specimens transferred by suitcase were held by a Cu clip affixed to a dual post cryogenic atom probe puck (Fig. S1). Alongside the clip of fibres, another Cu clip mounted with a flat coupon with Si posts was also placed on the same puck. The puck along with the clips was transferred under ultra-high vacuum by the suitcase. APT tips were prepared and coated with Cr [37,40]. In brief, a Cr lamella was lifted out, and a circular half-cut was introduced at a free edge (Fig. S2). The prepared APT specimen was positioned inside the half-cut at a zero-degree tilt. Subsequently, a semi-circular pattern with inner diameter 8 μm and outer diameter of 11 μm was placed on the cavity. To avoid cutting into the prepared specimen, a rectangle with disabled milling was positioned over the circular pattern. The milling was performed radially outwards with a current of 40 pA and 20 s. After completing the milling from one side, the Cr-lamella was retracted, and the stage was rotated by 90°, to access the other sides of the APT specimen. The same procedure was repeated to coat all four sides of the specimen effectively. APT experiments were conducted at a base temperature between 40 and 70 K, laser energy between 50 and 80 pJ (λ = 355 nm), and a detection rate of 2 ions per 1000 pulses. Out of twelve lithiated tips five yielded useful results, and out of seven delithiated tips three yielded useful results. APT data were reconstructed and processed with AP Suite and MATLAB.

3. Results and discussion

To analyse lithiated carbon fibres with atom probe tomography (APT) presented an even greater challenge than that of analysing uncycled carbon fibres [32,41]. The challenge originates in the stark contrast between Li and C, and the weak bond between them. For battery applications, the physiochemical stability of carbon materials and the electrochemical reactivity and fast mobility of Li are essential. However, due to the semi-conductivity of carbon fibres, the electrostatic field generated by the atom probe penetrates deep into the APT specimen and drives out Li to the tip surface [35]. Since the field strength necessary to induce field evaporation is a magnitude lower for Li → Li$^+$ than for C → C$^+$ [42], the Li migration to the surface is followed by massive evaporation of Li at low voltages before the voltage rises and C starts to evaporate (Fig. 1a).

In the three-dimensional reconstruction of a lithiated T800 carbon fibre, the massive field evaporation of Li manifests as an artifact: a cap of lithium on top of the carbon dominated volume (Fig. 1b). The carbon fibre is delithiated inside the atom probe instrument during the analysis. This leads to interesting implications of *in situ* delithiation [36]. During APT analysis, the sharp needle shaped specimen (end radius ~50 nm) is exposed to a high electric field (~10^{10} V/m). For semi-conductors such
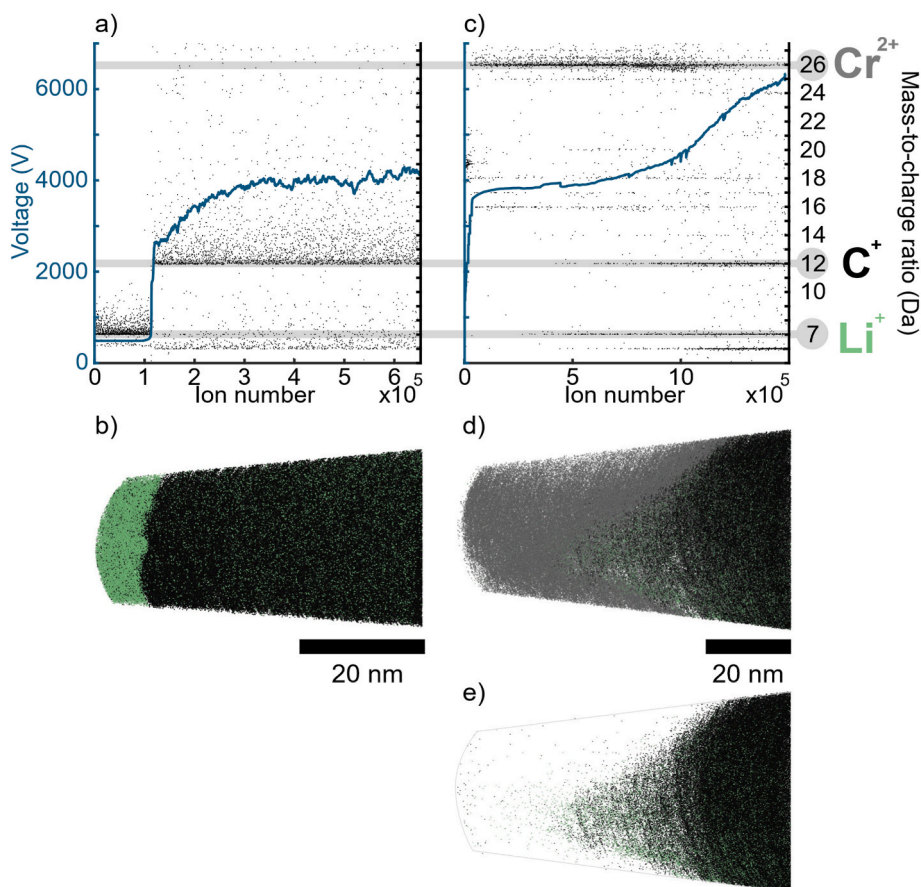
Fig. 1. Massive Li evaporation in the initial stage of APT analysis is suppressed with a field shielding Cr coating. a) Mass and voltage history of a bare lithiated carbon fibre with two stages: at the lowest voltage of 500 V with only Li hits; and at a higher voltage with foremost C hits. The continuous blue line represents the voltage history (left axis). Individual black dots represent ions with certain mass-to-charge ratio (right axis). b) Reconstruction with the massive evaporation of Li, which appears as a cap of Li ions (green) on a tip of predominantly C ions (black). c) Mass and voltage history of a Cr coated lithiated carbon fibre with no distinct separation of Li and C hits. Note that the first Li hits are among Cr, and still occur some time before the first C hit. Reconstructions d) with Cr ions (grey) and e) without Cr ions on a tip of lithiated carbon fibre. (A colour version of this figure can be viewed online.)

as carbon fibres, the electric field penetrates into the carbon fibre, which drives field-induced migration of Li. This has been proved with systematic experiments by Kim et al. and Pfeiffer et al. [35,36]. Kim [35] also indicated that employing a conductive coating on the top of the prepared APT specimens can circumvent this issue, which was suggested to provide a shielding effect against the penetration of the electrostatic field below the emitting surface. Through further exploration and optimization, Woods et al. [37] showed a successful and simple way of facilitating such metallic coatings on battery cathodes. Hence, we attempted to shield the APT specimens with a thin Cr layer on the tips as proposed by Woods et al. [37]. The metallic coating proved efficient in shielding the field, and the massive Li evaporation was supressed (Fig. 1c–e). Still, diffusion of Li occurred as a few Li ions were detected among Cr-related ions before the first C ions were detected (Fig. 1c). The diffusion may occur either before the analysis, i.e. during specimen preparation due to radiation damage from the high energy electrons (4 nA and 2 kV) or Ga$^+$ ions (3 nA and 30 kV), or during the APT analysis some Li ions diffuse along the shank surface to the tip. Since Li ions appear only after a quarter million ions, most likely it occurred during the specimen preparation.

To generate a reference value for the Li concentration in lithiated T800 carbon fibres, we made an estimate based on combining the information from the atomic composition of uncycled fibres and cycling data. APT on uncycled fibres according to our previously developed best practice [32] gave a composition of 96.6 at% C, 2.7 at% N, 0.7 at% O. This agrees with the data sheet of T800 that claims >96% C [43] and

previous APT results [19]. Ga implantation into the carbon fibre was observed in uncycled, lithiated, and delithiated carbon fibres. However, our results show that Li distribution seems independent of Ga distribution. According to the results of electrochemical cycling of T800 carbon fibres against Li metal, and in agreement with the literature [9], the T800 carbon fibres performed a specific capacity of 245 mAh/g (Fig. 2). The theoretical specific capacity of graphite (LiC$_6$) is 372 mAh/g, with a Li concentration of 14.3 at%. We estimate that fully lithiated T800 carbon fibres have the stoichiometry of LiC$_{8.8}$N$_{0.25}$O$_{0.06}$ and a Li concentration of 9.9 at% (see supplementary information). However, it is important to note that this is the lower bound of the concentration value, which assumes no Li from previous cycles is trapped in the fibre. Therefore, analysis of trapped Li is important, especially since trapped Li leads to capacity fade and loss in battery performance. However, estimating the amount of trapped Li in the fibre based solely on cycling data is precarious – Li is also consumed by the formation of the solid-electrolyte interphase (SEI) on the surface of the fibres. Discerning what part of the capacity fade in the cycling data is caused by SEI formation and what is caused by trapped Li is challenging. Thus, this motivates measurements by APT.

Mass spectra from APT experiments on Cr coated lithiated/delithiated carbon fibres (Fig. 3 and S3) were reminiscent of those of uncycled fibres, since they contain multiple molecular ions and peak overlaps [19], but with the additional peaks associated with Li and Cr (Fig. S4, Table S1, S2 and S3). The Cr coating was excluded from the analysis by isolating a cylinder-shaped region of interest (Φ 20 × 20 nm)
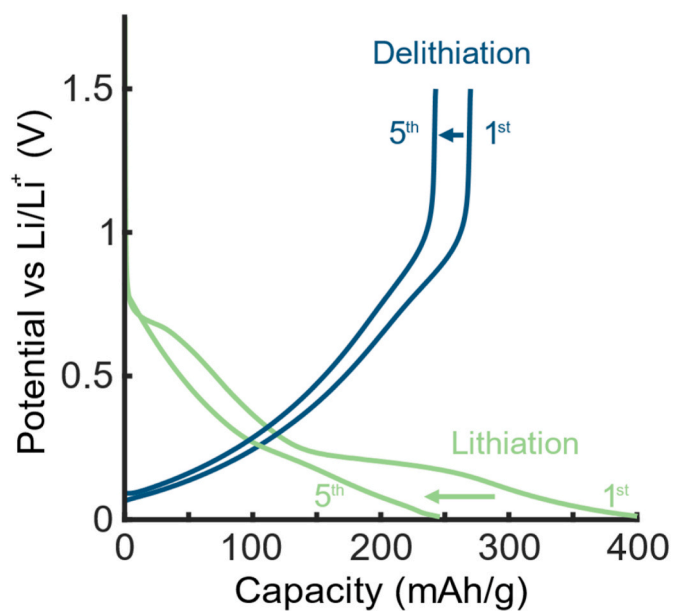
Fig. 2. First and fifth electrochemical cycles of carbon fibres against Li metal.

away from the coating and in the centre of the carbon fibre material. Nevertheless, it is apparent that during specimen preparation, some Cr was implanted in the carbonaceous bulk. The spectrum consists of multiple overlapping peaks which were deconvoluted based on the natural abundance of isotopes of Cr and C [32]. The significant amount of residual ion counts that were not accounted for by the isotope deconvolution were assigned as Li-related. The identification of Li-related peaks is further confirmed by their significant portion in the extracted volume in the centre of lithiated carbon fibre. This is evidenced by comparing the spectrum from the entire volume and that from the carbon fibre (Fig. 3). From the deconvoluted spectra of coated lithiated and delithiated carbon fibres, we calculated the atomic composition (Table 1). The distribution of O in the carbon fibres is rather homogenous, shown by the O atom maps in Fig. S5. Note, the chemical concentration and microstructure vary locally in both the uncycled and lithiated carbon fibre [17,19]. The values in Table 1 reflect the variation.

The average Li concentration of delithiated fibres was measured to 1.6 ± 0.2 at%, which indicates that Li is trapped inside the fibre. AES should be able to detect elements with concentrations in that range, but for analysis of delithiated carbon fibres, the Li concentration fell below the detection limit of the AES instrument [17]. This inconsistency is most probably due to difficulties in discerning very small Li_{KLL} peaks located in the slanted part at the low kinetic energy region of the AES spectrum [44]. APT could overestimate the Li concentration due to

surface migration from the shank. However, as discussed above, there is no indication of migration or diffusion of Li in the lithiated carbon fibres, owing to the electrostatic shielding by means of conductive coating. Furthermore, Li that was unambiguously detected by APT must come from the little volume of delithiated carbon fibre. The trapped Li in the carbon fibre is not involved in electrochemical cycling, and thus, together with the formation of SEI and other reactions, it is responsible for the initial capacity fade. Despite the heterogeneity within the distribution of trapped Li in carbon fibres and SEI, we can estimate the amount of initial capacity fade originating from the trapped Li in the fibre based on the APT measurement. The amount of Li trapped in a T800 carbon fibre (1.6 at%) corresponds to 35 mAh/g lost specific capacity (see supplementary information). In total, 155 mAh/g of specific capacity is lost during the first cycles (Fig. 2), which means that ~23 % of the capacity fade comes from Li trapped in the fibre, and the rest from the formation of SEI and other reactions.

With the now known amount of 1.6 at% trapped Li and the expected reversible 9.9 at% Li based on just the electrochemical cycling data, the expected total Li concentration in a fully lithiated carbon fibre is instead estimated to ~11.5 at%. However, the measured Li concentration of lithiated fibres only reaches 9.1 ± 0.3 at%. The discrepancy can be attributed to several reasons. Firstly, small Li transport into the Cr-coating seems to occur as evidenced by Fig. 1c. This likely occurred during the deposition of the Cr-coating via sputtering the Cr target with the energic Ga ions (30 kV). Some Cr land on the lithiated carbon fibre with relatively high energy, which drives a small amount of Li to migrate into the coating. The leeching of Li leads to a lower measured concentration. Secondly, the expected concentration is calculated based on the assumption that all fibres are equally lithiated. Thirdly, the deconvolution process of the relatively small data set is delicate and not entirely unambiguous. Finally, the sample preparation can also deplete the analysis volume of Li. During sample preparation in the FIB/SEM, the fibres were exposed to negative charges from the electron beam and positive charges from the ion beam. High current electron beams can attract Li to the surface of lithiated carbon materials, while ion beams displace Li [17,45,46]. During the shaping of APT tips from a small chunk of material in micrometre size into a sharp tip with tip radius < 50 nm, Li can be attracted to the surface by the electrons and then sputtered away by FIB, leading to the lower Li content.

A rough estimate of the spatial distribution of Li in the region of interest was made with 1D concentration profiles along the analysis axis (Fig. 4). The Li concentration appears uniform for both lithiated and delithiated fibres. This affirms that thanks to the shielding effect of the Cr coating, no remarkable preferential movement of Li during the APT experiment, which was manifested in cathode materials as irregular concentration profiles with elevated Li concentrations at the start of the reconstruction [35]. Additionally, no large agglomerates of Li were identified with iso-concentration surfaces. However, the crystallite size in T800 carbon fibres is around 2 nm [15], so a more detailed analysis
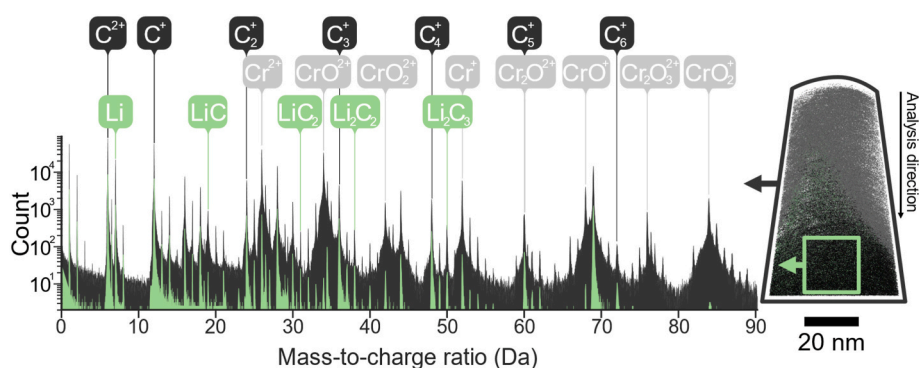

Fig. 3. Mass spectra of lithiated carbon fibre. The black coloured spectrum represents the full run, whereas the green coloured spectrum represents a cylinder-shaped region of interest (Φ 20 × 20 nm) at the centre of the APT tip away from the Cr coating. Some of the main peaks from C, Li, and Cr are marked.

Table 1
Atomic composition of uncycled, delithiated, and lithiated T800 carbon fibres, as measured by APT.

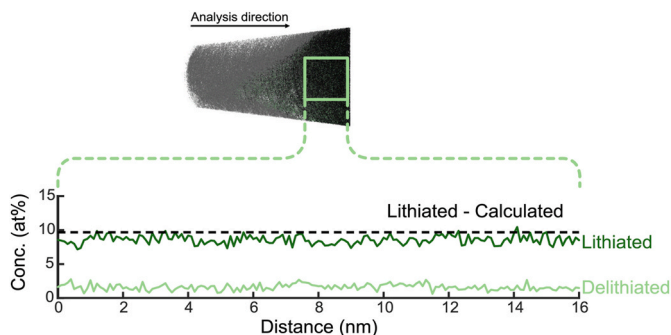| at. %	C	Li	N	O
Uncycled	96.6	-	2.7	0.7
Delithiated	94.4	1.6	2.4	1.6
Lithiated	86.6	9.1	2.9	1.4

Fig. 4. Li concentration profile for delithiated and lithiated carbon fibres along the analysis axis. Note that the Li content in lithiated carbon fibres fall below the expected value.

Fig. 5. Deconvolution of the peak at 7 Da. Superimposing linear spectra of single and multiple hits on the full spectrum reveals that the Li^+ is almost exclusively registered as single hits, whereas N^{2+} ions are part of multiple hits.

was required to study smaller agglomeration, which is discussed later.

Even though, natural isotopic abundance deconvolution can determine the contribution from a specific ion species to a mass-to-charge peak and provide more accurate compositional information, it is not able to spatially differentiate specific ions. This limitation hampers analysis of the spatial distribution of Li-related ions. Typically, the obstacle is circumvented by only analysing the spatial distribution of ions from peaks without overlap and assume that those ions' spatial properties are also representative of the ions set aside. However, no Li-containing peak was without potential overlap. The peak at 7 Da is the largest source of Li in the spectrum but overlaps with a N-containing peak. Still, there is a slight difference in their peak positions: Li^+ has a mass-to-charge ratio of 7.02 Da, and N^{2+} of 7.00 Da [47]. This peak shift is enough to discern the two peaks (Fig. 5), but the issue of spatial differentiation remains, as the peaks still partially overlap. One can of course introduce a dividing line between the peaks and assign ions with lower mass-to-charge ratio as N^{2+} and higher mass-to-charge ratio as Li^+. However, this is an approach that will assign some ions incorrectly due to the ions in the thermal tails in the spectrum. Fortunately, the two ion types experience different evaporation conditions: Li^+ evaporates as single ions, while N^{2+} reaches the detector in multi hit events (Fig. 5). The massive Li evaporation at the initial stage only consist of Li and has 98 % single hits, which further suggests that Li evaporates as single ions. We utilised this, and deconvoluted the 7 Da peak by single and multiple hits. Thus, all the single hits were assigned to represent Li. The approach of single/multiple hits deconvolution can be even more powerful as it can be used for peak identification in the case of weaker signals that otherwise could be mistaken for background (Fig. S6).

We evaluated agglomerations of Li with frequency distribution analysis (Fig. 6a–d). The region of interest was split in bins containing 100 ions each. The composition in each bin was calculated and then plotted as histograms. If the distribution is random and free of agglomerates the histogram will follow a binomial distribution [48]. On the other hand, if the measured data deviates from the binomial distribution the null hypothesis "*the ions are distributed randomly throughout*
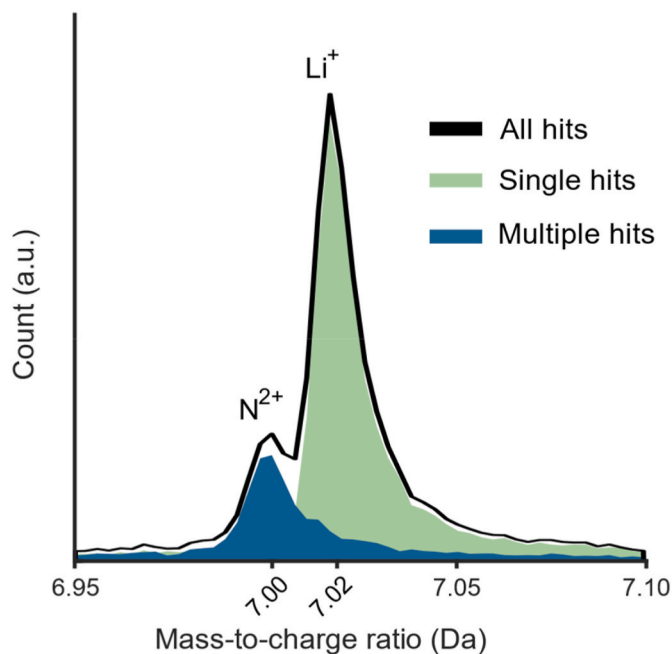
the data set" can be rejected, indicating some sort of solute separation. The deviation can be quantified with Pearson coefficient, μ, which is a value between 0 and 1. A random distribution has a Pearson coefficient close to 0. The frequency distribution analysis of $^7Li^+$ and $^{12}C^+$ in a delithiated sample yields $\mu_{Li} = 0.15$ and $\mu_C = 0.17$, which indicates that Li distribution is close to random. For a lithiated sample, though, the coefficients are $\mu_{Li} = 0.49$ and $\mu_C = 0.17$. The Li distribution here is thus farther from random.

The frequency distribution analysis suggests greater solute agglomeration in lithiated fibres compared to delithiated fibres. One possible explanation for the even distribution of Li in the delithiated fibres is due to the diffusion at low states of lithiation. For graphite at low states of lithiation, Li diffusion is predicted to be faster due to a low activation energy of 0.05 eV compared to 0.51 eV for high states of lithiation [49, 50]. However, electrochemical impedance spectroscopy (EIS) on IMS65 carbon fibres indicated slower diffusion at low states of lithiation [10]. Nevertheless, in order to investigate the Li distribution within minutes after delithiation of the material, we returned to the *in situ* delithiated fibres without Cr coating (Fig. 1b). The Li concentration in the delithiated part is 1.4 at%, which is close to the level obtained from Cr-coated delithiated fibres. The Li concentration in the part consisting of only Li from the initial stage is of course 100 at%. Combining the ion counts from the two regions gives a Li concentration of 10.3 at%
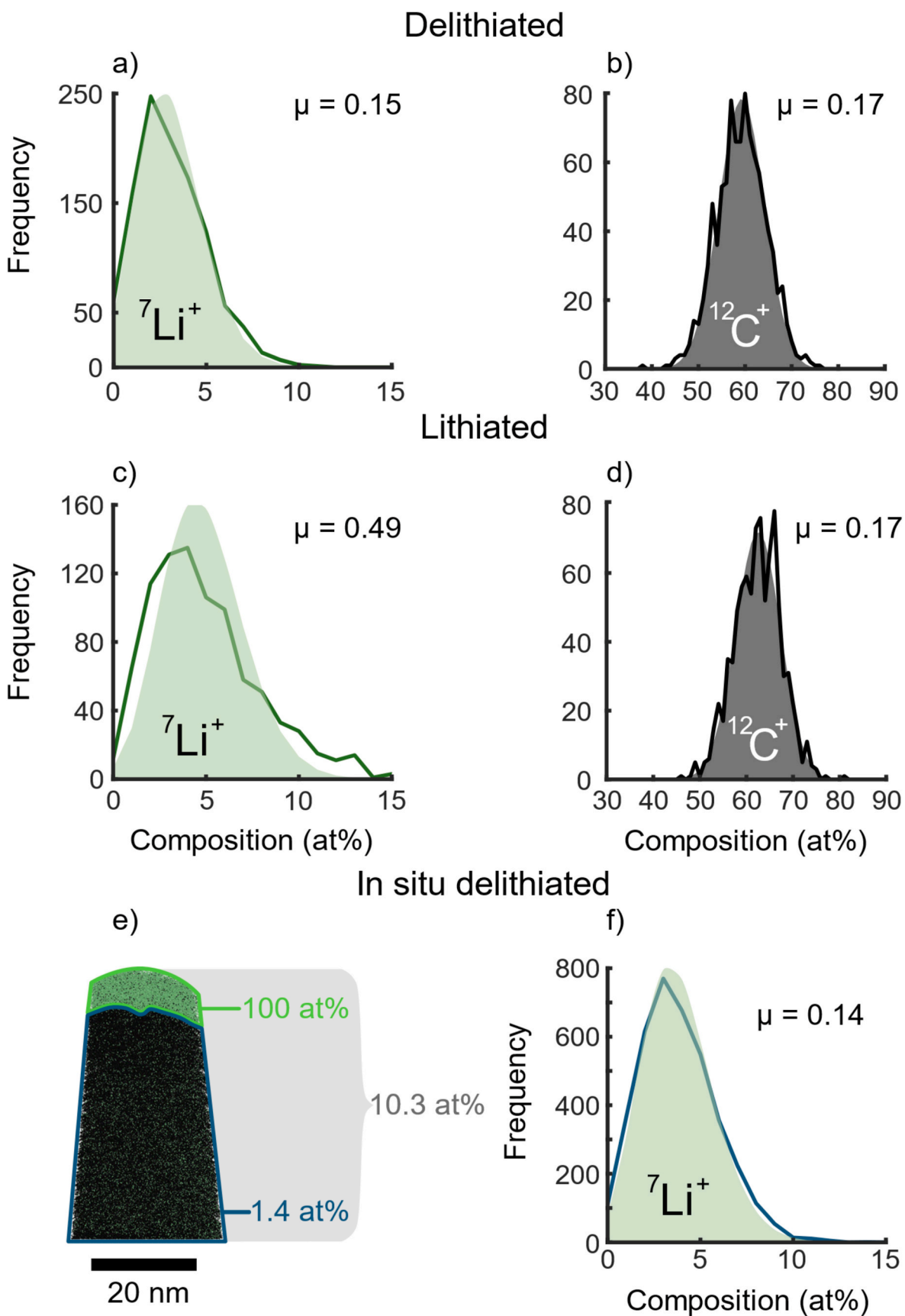
Fig. 6. Frequency distribution diagrams (line represents measured data, and shaded region the binomial distribution) with corresponding Pearson coefficient, μ, for a) $^7Li^+$ and b) $^{12}C^+$ in delithiated carbon fibres, and c) $^7Li^+$ and d) $^{12}C^+$ in lithiated carbon fibres. A Pearson coefficient close to 0 indicates an even spatial distribution of ions. e) Reconstruction of *in situ* delithiated carbon fibre showing the Li concentration in the Li cap, in the bulk of the carbon fibre, and in the total volume. f) Frequency distribution diagram of $^7Li^+$ in the bulk of the delithiated carbon fibre.

(Fig. 6e), which is rather close to the Cr-coated lithiated fibres. An assumption that the sample has experienced similar delithiation process inside the APT instrument as the fibre does during cycling, seems reasonable based on these measured concentrations. Thus, a frequency distribution analysis of the *in situ* delithiated sample is a fair method to determine the level of solute agglomeration of Li immediately after delithiation (Fig. 6f). The Pearson coefficient for $^7Li^+$ in the *in situ* delithiated T800 is $\mu_{Li} = 0.14$, which reaffirms that in a delithiated state, the spatial distribution of Li is close to random. It also indicates that no Li diffusion occurred in the Cr-coated delithiated fibres.

At this point the Li agglomeration in lithiated fibres could be explained by a mechanism dependent on either crystalline/amorphous domains or N heteroatoms. To analyse the effect of N heteroatoms on the Li distribution, we employed nearest neighbour analysis [51]. Here the 7 Da peak was deconvoluted based on mass-to-charge ratio. For each Li atom the distance to its nearest N atom was measured and plotted in a histogram (Fig. 7). In the same plot we added a histogram for the calculated nearest neighbour distances for a system of randomly distributed atoms. Thus, by comparing the measured histogram with the calculated histogram, we can determine whether the Li distribution is influenced by or independent of proximity to N. The more a measured histogram adheres to the calculated histogram, the closer the distribution of atoms is to a random system without proximity dependence. The analysis showed that in delithiated carbon fibres the proximity of N and Li follows the expected distribution for a randomised system (Fig. 7a). Therefore, there is no indication that N heteroatoms are responsible for the distribution of Li trapped in delithiated carbon fibres. Similarly, in lithiated carbon fibres the position of Li atoms is independent of the proximity to N atoms (Fig. 7b). Furthermore, radial distribution function analysis of the N concentration as a function of radial distance from each Li atom showed no concentration peak (Fig. S7). Thus, it is evident that Li atoms coordinate independently of the vicinity to N heteroatoms. However, this does not discredit the effect of N on electrochemical performance of carbon fibres, since the defects in the carbonaceous microstructure induced by heteroatoms still may lead to favourable properties such as transport paths through the otherwise virtually impermeable graphene layers.

Thanks to the nature of field evaporation of Li – $^7Li^+$ are readily distinguished as single hit ions with no overlap and form the most predominant Li-containing peak – we can use $^7Li^+$ to perform detailed frequency distribution analysis and nearest neighbour analysis. On the other hand, despite their relatively low level, the Li-containing molecular ions can influence the analysis results, which is not counted in this study.

This leaves the Li agglomeration in lithiated fibres to be explained with crystalline/amorphous domains. Presumably, the agglomerated distribution (Fig. 6c) shows that the Li concentration is higher in one domain, and lower in the other. It has been shown that during the lithiation process, Li is first inserted into the more amorphous domains of the carbon fibre and at the later stage in the more crystalline domains.

The sequence of lithium insertion into different domains has been evidenced by analysing carbon fibres with different charge states using NMR and AES, respectively [16,17]. We are not able, with APT, to conclusively determine which domain is rich in Li. Still, it is reasonable to ascribe it to the amorphous domain, since this is the domain first experiencing Li insertion, and thus being the preferred domain for Li to insert into. This means that the crystalline domain is less accessible to Li. The stacking of graphene layers in the crystallites is not perfectly graphitic, but turbostratic, and known to be less capable of hosting Li [52]. Furthermore, fibres with large crystallites perform worse electrochemically [15]. Hence, we identify key for enhancing the electrochemical capacity of carbon fibres to be modification of the crystalline domains. It should also be kept in mind that the size and alignment of the crystallites also influence mechanical properties [53,54]. The design of crystallites can take two routes. The first option is to make the crystallites smaller. A higher ratio of amorphous domains leads to greater capacity, but also decreased stiffness. The second option is instead changing the graphene stacking to be less turbostratic and more ordered towards graphitic. However, in carbon fibre manufacture practice, increased graphitisation is closely linked to the growth of the crystallites, which means shrinkage of the amorphous domain and consequently its usefulness for the electrochemical capacity. Additionally, the feasibility of achieving crystallites with graphitic stacking in carbon fibres is dubious. Using the interplanar spacing as a measure of graphitisation, carbon fibres with highly ordered crystallites only reach 3.47 Å [15], which is far from the tight packing of pure graphite at 3.35 Å [13]. Nevertheless, even though it is challenging to achieve from a purely practical point of view, small and yet highly graphitic crystallites will likely be beneficial for multifunctional carbon fibres in structural batteries. Finally, the diffusion rate of Li in different domains is out of the scope of this study, but still crucial for structural batteries.

4. Conclusion

We analysed lithiated/delithiated PAN-based T800 carbon fibres with APT. Challenges with massive evaporation of Li and subsequent *in situ* delithiation were overcome by shielding the APT tips from deep field penetration with Cr-coating. Spectral deconvolution gave atomic composition of ~9 at% Li, which is close to the theoretical values for lithiated fibres. We also revealed the amount of Li trapped inside the fibres after delithiation to be ~1.5 at%, which is responsible for a significant part (~25%) of the initial capacity fade that carbon fibres experience during electrochemical cycling. The spatial distribution of Li was quantified with frequency distribution diagrams and Pearson coefficients. At the delithiated state, Li is uniformly distributed, but at full lithiation state, solute agglomeration of Li is detected. Furthermore, nearest neighbour and radial distribution function analysis showed that the distribution of Li atoms is independent of N heteroatoms. These findings extend the knowledge of the electrochemically active carbon fibres for multifunctional energy storage and aids the advancement of
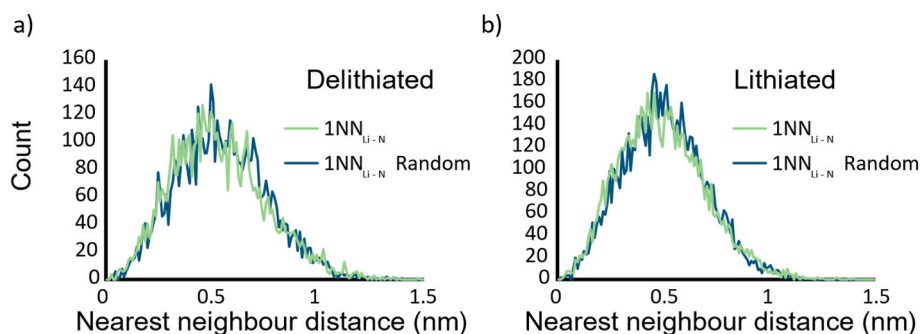

Fig. 7. Nearest neighbour analysis of the distribution of distances separating each Li and its nearest N in a) delithiated and b) lithiated carbon fibres. The experimental distribution in both cases coincide with the expected distances in a randomised system.

structural battery technology. This study also shows that it is possible to investigate lithiated carbonaceous materials with APT and map the distribution of Li.

CRediT authorship contribution statement

M. Johansen: Writing – original draft, Visualization, Software, Methodology, Investigation, Formal analysis, Data curation, Conceptualization. **M.P. Singh:** Writing – review & editing, Methodology, Investigation, Data curation. **J. Xu:** Resources, Writing – review & editing. **L.E. Asp:** Writing – review & editing, Resources. **B. Gault:** Writing – review & editing, Supervision, Methodology, Resources. **F. Liu:** Project administration, Methodology, Funding acquisition, Formal analysis, Conceptualization, Supervision, Writing – original draft.

Declaration of competing interest

The authors declare that they have no known competing financial interests or personal relationships that could have appeared to influence the work reported in this paper.

Acknowledgment

Appendix A. Supplementary data

Supplementary data to this article can be found online at https://doi.org/10.1016/j.carbon.2024.119091.

References

[1] L.E. Asp, M. Johansson, G. Lindbergh, J. Xu, D. Zenkert, Structural battery composites: a review, Funct. Compos. Struct. 1 (4) (2019), https://doi.org/10.1088/2631-6331/ab5571.

[2] L.E. Asp, K. Bouton, D. Carlstedt, S. Duan, R. Harnden, W. Johannisson, et al., A structural battery and its multifunctional performance, Adv. Energy Sustain. Res. 2000093 (2021), https://doi.org/10.1002/aesr.202000093.

[3] J. Xu, Z. Geng, M. Johansen, D. Carlstedt, S. Duan, T. Thiringer, et al., A multicell structural battery composite laminate, EcoMat 4 (3) (2022) 1–11, https://doi.org/10.1002/eom2.12180.

[4] L.E. Asp, E.S. Greenhalgh, Structural power composites, Compos. Sci. Technol. 101 (2014) 41–61, https://doi.org/10.1016/j.compscitech.2014.06.020.

[5] W. Johannisson, D. Zenkert, G. Lindbergh, Model of a structural battery and its potential for system level mass savings, Multifunctional Mater. 2 (3) (2019), https://doi.org/10.1088/2399-7532/ab3bdd.

[6] M.S. Siraj, S. Tasneem, D. Carlstedt, S. Duan, M. Johansen, C. Larsson, et al., Advancing structural battery composites: robust manufacturing for enhanced and consistent multifunctional performance, Adv. Energy Sustain. Res. 2300109 (2023), https://doi.org/10.1002/aesr.202300109.

[7] G.J.H. Lim, K.K. Chan, N.A.A. Sutrisnoh, M. Srinivasan, Design of structural batteries: carbon fibers and alternative form factors, Mater. Today Sustain. 20 (2022) 100252, https://doi.org/10.1016/j.mtsust.2022.100252.

[8] K. Moyer, C. Meng, B. Marshall, O. Assal, J. Eaves, D. Perez, et al., Carbon fiber reinforced structural lithium-ion battery composite: multifunctional power integration for CubeSats, Energy Storage Mater. 24 (2020) 676–681, https://doi.org/10.1016/j.ensm.2019.08.003. April 2019.

[9] J. Hagberg, S. Leijonmarck, G. Lindbergh, High precision coulometry of commercial PAN-based carbon fibers as electrodes in structural batteries, J. Electrochem. Soc. 163 (8) (2016) A1790–A1797, https://doi.org/10.1149/2.0041609jes.

[10] M.H. Kjell, T.G. Zavalis, M. Behm, G. Lindbergh, Electrochemical characterization of lithium intercalation processes of PAN-based carbon fibers in a microelectrode system, J. Electrochem. Soc. 160 (9) (2013) A1473–A1481, https://doi.org/10.1149/2.054309jes.

[11] M.H. Kjell, E. Jacques, D. Zenkert, PAN-based carbon fiber negative electrodes for structural lithium-ion batteries 158 (12) (2011) 1455–1460, https://doi.org/10.1149/2.053112jes.

[12] J. Xu, C. Creighton, M. Johansen, F. Liu, S. Duan, D. Carlstedt, et al., Effect of tension during stabilization on carbon fiber multifunctionality for structural battery composites, Carbon N Y 209 (March) (2023) 117982, https://doi.org/10.1016/j.carbon.2023.03.057. Jun.

[13] J.-B. Donnet, T.W. Wang, S. Rebouillat, J.C.M. Peng, Carbon Fibres, third ed., Marcel Dekker Inc., 1998.

[14] S. Park, Carbon Fibers, second ed., Springer Nature, 2018.

[15] G. Fredi, S. Jeschke, A. Boulaoued, J. Wallenstein, M. Rashidi, F. Liu, et al., Graphitic microstructure and performance of carbon fibre Li-ion structural battery electrodes, Multifunctional Mater. 1 (1) (2018) 015003, https://doi.org/10.1088/2399-7532/aab707.

[16] Y. Fang, K. Peuvot, A. Gratrex, E.V. Morozov, J. Hagberg, G. Lindbergh, et al., Lithium insertion in hard carbon as observed by 7Li NMR and XRD. The local and mesoscopic order and their relevance for lithium storage and diffusion, J Mater Chem A Mater (10) (2022) 10069–10082, https://doi.org/10.1039/d2ta00078d.

[17] M. Johansen, J. Xu, P.L. Tam, L.E. Asp, F. Liu, Lithiated carbon fibres for structural batteries characterised with Auger electron spectroscopy, Appl. Surf. Sci. 627 (April) (2023) 157323, https://doi.org/10.1016/j.apsusc.2023.157323. Aug.

[18] S. Hofmann, *Auger- and X-ray photoelectron Spectroscopy in materials science*, vol. 49, in: Springer Series in Surface Sciences vol. 49, Springer Berlin Heidelberg, Berlin, Heidelberg, 2013, https://doi.org/10.1007/978-3-642-27381-0.

[19] M. Johansen, C. Schlueter, P.L. Tam, L.E. Asp, F. Liu, Mapping nitrogen heteroatoms in carbon fibres using atom probe tomography and photoelectron spectroscopy, Carbon N Y 179 (2021) 20–27, https://doi.org/10.1016/j.carbon.2021.03.061.

[20] A.L.M. Reddy, A. Srivastava, S.R. Gowda, H. Gullapalli, M. Dubey, P.M. Ajayan, Synthesis of nitrogen-doped graphene films for lithium battery application, ACS Nano 4 (11) (2010) 6337–6342, https://doi.org/10.1021/nn101926g.

[21] P. Han, Y. Yue, L. Zhang, H. Xu, Z. Liu, K. Zhang, et al., Nitrogen-doping of chemically reduced mesocarbon microbead oxide for the improved performance of lithium ion batteries, Carbon N Y 50 (3) (2012) 1355–1362, https://doi.org/10.1016/j.carbon.2011.11.007.

[22] Z. Xing, Z. Ju, Y. Zhao, J. Wan, Y. Zhu, Y. Qiang, et al., One-pot hydrothermal synthesis of Nitrogen-doped graphene as high-performance anode materials for lithium ion batteries, Sci. Rep. 6 (April) (2016) 1–10, https://doi.org/10.1038/srep26146.

[23] M. Inagaki, M. Toyoda, Y. Soneda, T. Morishita, Nitrogen-doped carbon materials, Carbon N Y 132 (2018) 104–140, https://doi.org/10.1016/j.carbon.2018.02.024.

[24] Z. He, M. Li, Y. Li, L. Wang, J. Zhu, W. Meng, et al., Electrospun nitrogen-doped carbon nanofiber as negative electrode for vanadium redox flow battery, Appl. Surf. Sci. 469 (2019) 423–430, https://doi.org/10.1016/j.apsusc.2018.10.220. September 2018.

[25] X. Wang, Q. Weng, X. Liu, X. Wang, D. Tang, W. Tian, et al., Atomistic origins of high rate capability and capacity of N-doped graphene for lithium storage, Nano Lett. 14 (3) (2014) 1164–1171, https://doi.org/10.1021/nl4038592.

[26] B. Zhang, Y. Yu, Z.-L. Xu, S. Abouali, M. Akbari, Y.-B. He, et al., Correlation between atomic structure and electrochemical performance of anodes made from electrospun carbon nanofiber films, Adv. Energy Mater. 4 (7) (2014), https://doi.org/10.1002/aenm.201301448.

[27] Y.F. Li, Z. Zhou, L.B. Wang, CNx nanotubes with pyridinelike structures: p-type semiconductors and Li storage materials, J. Chem. Phys. 129 (10) (2008), https://doi.org/10.1063/1.2975237.

[28] T. Schiros, D. Nordlund, Lucia Pálová, D. Prezzi, L. Zhao, K.S. Kim, et al., Connecting dopant bond type with electronic structure in n-doped graphene, Nano Lett. 12 (8) (2012) 4025–4031, https://doi.org/10.1021/nl301409h.

[29] F. Wang, J. Graetz, M.S. Moreno, C. Ma, L. Wu, V. Volkov, et al., Chemical distribution and bonding of lithium in intercalated graphite: identification with optimized electron energy loss spectroscopy, ACS Nano 5 (2) (2011) 1190–1197, https://doi.org/10.1021/nn1028168.

[30] Z.W. Yin, W. Zhao, J. Li, X.X. Peng, C. Lin, M. Zhang, et al., Advanced electron energy loss spectroscopy for battery studies, Adv. Funct. Mater. 32 (1) (2022), https://doi.org/10.1002/adfm.202107190.

[31] B. Gault, A. Chiaramonti, O.C. Mirédin, P. Stender, R. Dubosq, C. Freysoldt, et al., Atom probe tomography, Nat. Rev. Methods Prim. 1 (1) (2021) 51, https://doi.org/10.1038/s43586-021-00047-w. Jul.

[32] M. Johansen, F. Liu, Best practices for analysis of carbon fibers by atom probe tomography, Microsc. Microanal. 28 (4) (2022) 1092–1101, https://doi.org/10.1017/S1431927621012812.

[33] D. Santhanagopalan, D.K. Schreiber, D.E. Perea, R.L. Martens, Y. Janssen, P. Khalifah, et al., Effects of laser energy and wavelength on the analysis of LiFePO₄ using laser assisted atom probe tomography, Ultramicroscopy 148 (2015) 57–66, https://doi.org/10.1016/j.ultramic.2014.09.004.

[34] G.H. Greiwe, Z. Balogh, G. Schmitz, Atom probe tomography of lithium-doped network glasses, Ultramicroscopy 141 (2014) 51–55, https://doi.org/10.1016/j.ultramic.2014.03.007.

[35] S.H. Kim, S. Antonov, X. Zhou, L.T. Stephenson, C. Jung, A.A. El-Zoka, et al., Atom probe analysis of electrode materials for Li-ion batteries: challenges and ways forward, J Mater Chem A Mater 10 (9) (2022) 4926–4935, https://doi.org/10.1039/d1ta10050e.

[36] B. Pfeiffer, J. Maier, J. Arlt, C. Nowak, In situ atom probe deintercalation of lithium-manganese-oxide, Microsc. Microanal. 23 (2) (2017) 314–320, https://doi.org/10.1017/S1431927616012691.

[37] E. Woods, M.P. Singh, S.H. Kim, T.M. Schwarz, J.O. Douglas, A.A. El-Zoka, et al., A versatile and reproducible cryo-sample preparation methodology for atom probe studies, Microsc. Microanal. (2023), https://doi.org/10.1093/micmic/ozad120. Oct.

[38] T.M. Schwarz, E. Woods, M.P. Singh, C. Jung, L.S. Aota, K. Jang, et al., In-situ metallic coating of atom probe specimen for enhanced yield, performance, and increased field-of-view, Sep, http://arxiv.org/abs/2309.07836, 2023.

[39] M.P. Singh, E. Woods, S.-H. Kim, C. Jung, L.S. Aota, B. Gault, Facilitating the Systematic Nanoscale Study of Battery Materials by Atom Probe Tomography through In-situ Metal Coating, Batter Supercaps, 2023, https://doi.org/10.1002/batt.202300403. Nov.

[40] M.P. Singh, E. V Woods, S.H. Kim, C. Jung, L.S. Aota, B. Gault, Facilitating the systematic nanoscale study of battery materials by atom probe tomography through in-situ metal coating, Sep, http://arxiv.org/abs/2309.07842, 2023.

[41] R.K.W. Marceau, A.S. Taylor, T. Sato, S.P. Ringer, B.L. Fox, N. Stanford, L. C. Henderson, et al., Local electrode atom probe tomography of carbon fibre, Microsc. Microanal. 25 (S2) (2019) 2496–2497, https://doi.org/10.1017/s1431927619013217.

[42] T.T. Tsong, Field ion image formation, Surf. Sci. 70 (1) (1978) 211–233, https://doi.org/10.1016/0039-6028(78)90410-7.

[43] T800S intermediate modulus carbon fiber [Online]. Available, https://www.toraycma.com/. (Accessed 30 November 2020).

[44] M. Hoffmann, M. Zier, S. Oswald, J. Eckert, Challenges for lithium species identification in complementary Auger and X-ray photoelectron spectroscopy, J. Power Sources 288 (2015) 434–440, https://doi.org/10.1016/j.jpowsour.2015.04.144.

[45] Y. Zhang, W. Zhai, X. Hu, Y. Jiang, S. Chen, Y. Zhang, et al., Application of Auger electron spectroscopy in lithium-ion conducting oxide solid electrolytes, Nano Res. 3 (2022) 1–10, https://doi.org/10.1007/s12274-022-4431-2.

[46] L.T. Belkacemi, B. Gault, V.A. Esin, J. Epp, Ga-induced delithiation of grain boundaries in a Li containing Al-based alloy, Mater. Char. 199 (March) (2023) 112812, https://doi.org/10.1016/j.matchar.2023.112812.

[47] P. Biévre, M. Gallet, N.E. Holden, I.L. Barnes, Isotopic abundances and atomic weights of the elements, J. Phys. Chem. Ref. Data 13 (3) (1984) 809–891, https://doi.org/10.1063/1.555720.

[48] M.P. Moody, L.T. Stephenson, A.V. Ceguerra, S.P. Ringer, Quantitative binomial distribution analyses of nanoscale like-solute atom clustering and segregation in atom probe tomography data, Microsc. Res. Tech. 71 (7) (2008) 542–550, https://doi.org/10.1002/jemt.20582.

[49] H. Zhang, Y. Yang, D. Ren, L. Wang, X. He, Graphite as anode materials: fundamental mechanism, recent progress and advances, Energy Storage Mater. 36 (October 2020) (2021) 147–170, https://doi.org/10.1016/j.ensm.2020.12.027.

[50] Q. Liu, S. Li, S. Wang, X. Zhang, S. Zhou, Y. Bai, et al., Kinetically determined phase transition from stage II (LiC12) to stage i (LiC6) in a graphite anode for Li-ion batteries, J. Phys. Chem. Lett. 9 (18) (2018) 5567–5573, https://doi.org/10.1021/acs.jpclett.8b02750.

[51] A. Shariq, T. Al-Kassab, R. Kirchheim, R.B. Schwarz, Exploring the next neighbourhood relationship in amorphous alloys utilizing atom probe tomography, Ultramicroscopy 107 (9) (2007) 773–780, https://doi.org/10.1016/j.ultramic.2007.02.030.

[52] J.R. Dahn, T. Zheng, Y. Liu, J.S. Xue, Mechanisms for lithium insertion in carbonaceous materials, Science 270 (5236) (1979) 590–593, https://doi.org/10.1126/science.270.5236.590. Oct. 1995.

[53] D.J. Johnson, Structure-property relationships in carbon fibres, J. Phys. D Appl. Phys. 20 (3) (1987) 286–291, https://doi.org/10.1088/0022-3727/20/3/007.

[54] X. Huang, Fabrication and properties of carbon fibers, Materials 2 (4) (2009) 2369–2403, https://doi.org/10.3390/ma2042369.